FAP106 is an interaction hub required for assembly of conserved and lineage-specific microtubule inner proteins at the cilium inner junction

[a]Michelle M. Shimogawa, [a]Angeline S. Wijono, [a,b,c]Hui Wang, [a,c,e]Jiayan Zhang, [d]Jihui Sha, [a]Natasha Szombathy, [a]Sabeeca Vadakkan, [a]Paula Pelayo, [a]Keya Jonnalagadda, [d]James Wohlschlegel, [a,c,e]Z. Hong Zhou*, and [a,c,e]Kent L. Hill*

[a]Department of Microbiology, Immunology and Molecular Genetics, University of California Los Angeles, Los Angeles, CA, 90095

[b]Department of Bioengineering, University of California Los Angeles, Los Angeles, CA, 90095

[c]California NanoSystems Institute, University of California Los Angeles, Los Angeles, CA, 90095

[d]Department of Biological Chemistry, University of California Los Angeles, Los Angeles, CA, 90095

[e]Molecular Biology Institute, University of California Los Angeles, Los Angeles, CA, 90095

Running title: *T. brucei* MIPs

*Corresponding authors:

Kent L. Hill

609 Charles E. Young Drive E, MSB 1602-G, Los Angeles, CA 90095

kenthill@microbio.ucla.edu

Z. Hong Zhou

CNSI 5511C, 570 Westwood Plaza, Los Angeles, CA 90095

Hong.Zhou@UCLA.edu

Author contributions

Designed research: MS, AW, HW, JZ, HZ, KH

Performed research: MS, AW, HW, JZ, JS, NS, SV, PP, KJ

Contributed new reagents or analytic tools:

Analyzed data: MS, AW, HW, JZ, JS, NS, SV, PP, KJ, JW, HZ, KH

Wrote the paper: MS, AW, HW, HZ, KH

ABSTRACT

Motility of pathogenic protozoa depends on flagella (synonymous with cilia) with axonemes containing nine doublet microtubules (DMTs) and two singlet microtubules. Microtubule inner proteins (MIPs) within DMTs influence axoneme stability and motility and provide lineage-specific adaptations, but individual MIP functions and assembly mechanisms are mostly unknown. Here, we show in the sleeping sickness parasite *Trypanosoma brucei*, that FAP106, a conserved MIP at the DMT inner junction, is required for trypanosome motility and functions as a critical interaction hub, directing assembly of several conserved and lineage-specific MIPs. We further use comparative cryogenic electron tomography (cryoET) and quantitative proteomics to identify novel MIP candidates, and RNAi knockdown plus fitting of AlphaFold models into cryoET maps to demonstrate one of these, MC8, is a trypanosome-specific MIP required for parasite motility. Our work advances understanding of MIP assembly mechanisms and identifies lineage-specific motility proteins that are attractive targets to consider for therapeutic intervention.

INTRODUCTION

Cilia (synonymous with eukaryotic flagella) are conserved, microtubule-based structures that provide motility and signaling functions at the surface of eukaryotic cells. Cilium motility is required for normal human reproduction, development, physiology, and to combat infection (1). Motile cilia also drive cell propulsion in eukaryotic pathogens responsible for tremendous human suffering worldwide (2, 3). Given this broad distribution and central importance to eukaryote cell biology and human health, understanding structural foundations of cilium assembly and motility is of broad interest.

Most motile cilia are built around a "9 + 2" cylindrical axoneme consisting of nine doublet microtubules (DMTs) surrounding a central pair of singlet microtubules. Each DMT is comprised

26 of a complete, 13-protofilament A-microtubule (A-tubule) and a partial, 10-protofilament B-
27 microtubule (B-tubule), with non-tubulin proteins forming an “inner junction” (IJ) filament that
28 connects the A- and B-tubules (4, 5). Recent studies have revealed a previously unappreciated,
29 yet universal feature of motile axonemes, showing that DMTs are not hollow but, instead, are
30 lined with a highly organized network of interconnected “microtubule inner proteins” (MIPs) (6-
31 9). Structures inside DMTs had been reported several decades ago in flagellated protozoa (10,
32 11), but the diversity and ubiquitous distribution of such structures was not recognized until
33 cryogenic electron tomography (cryoET) enabled high-resolution, 3D structural analysis (8, 12).
34 Studies in organisms from diverse eukaryotic lineages (13-17) indicate MIPs are present in both
35 the A- and B-tubules and occur in a regularly repeating pattern along the length of the DMT in
36 all motile axonemes. Their broad taxonomic distribution indicates MIPs are fundamentally
37 important for axoneme function and likely were present prior to eukaryote diversification.
38 Meanwhile, absence of regularly spaced MIP structures in non-motile cilia (18, 19) suggests
39 they are required specifically for motile axonemes. Recent work has shown MIPs can influence
40 axoneme stability, structure and beating (13, 14, 16, 20-23). Nonetheless, many aspects of MIP
41 functions and assembly mechanisms remain poorly understood.

42 In recent, groundbreaking work, cryogenic electron microscopy (cryoEM) was used to
43 reconstruct near-atomic resolution structures of the axoneme, thereby allowing *in situ*
44 identification and atomic modeling of MIPs in *Chlamydomonas*, *Tetrahymena,* and mammals
45 (13, 16, 17, 20, 24). These studies have expanded opportunities for studying MIP function and
46 revealed that while some MIPs are conserved across diverse taxa, others represent lineage-
47 specific adaptations (13, 16, 17, 20, 24). Axonemes of diverse organisms share general
48 architecture and beating mechanism, and lineage-specific MIPs therefore offer a potential
49 mechanism for meeting organism-specific motility characteristics (2, 15, 25), such as those

50 presented by movement of parasitic protozoa through tissues of their human and animal hosts
51 (26, 27). Identification and analysis of lineage-specific MIPs are therefore of great interest.

52 African trypanosomes, e.g. *Trypanosoma brucei* and related kinetoplastids, are
53 flagellated, protozoan pathogens that cause extensive human suffering and limit economic
54 development in some of the world's poorest regions (28, 29). Trypanosomes also represent
55 diverse eukaryotic lineages that have proven useful for uncovering novel features of eukaryote
56 biology (30, 31). *T. brucei* motility exhibits several distinctive features that support movement
57 through host tissues (15, 32) and is required for pathogenesis (33) and transmission (34). The
58 *T. brucei* flagellum has a large and diverse repertoire of MIP structures, including several that
59 are lineage-specific, particularly in the B-tubule (15). Except for a few conserved examples,
60 however, proteins comprising most *T. brucei* MIP structures are unknown, representing a critical
61 knowledge gap in *T. brucei* flagellum assembly and motility.

62 FAP106/ENKUR is a conserved B-tubule MIP that is required for motility of mammalian
63 sperm (35) and occupies a key position in the B-tubule, spanning the IJ filament and
64 interconnecting several other MIPs (13, 16, 20, 36). However, the structural foundation of the
65 FAP106/ENKUR motility defect is unknown, and the role of FAP106 in assembly of the IJ and
66 other MIPs has not been examined. To address these questions, we used RNAi knockdown to
67 investigate FAP106 function in *T. brucei* and show that FAP106 is required for parasite motility
68 and normal flagellum length. Combining CryoET and tandem mass tag (TMT) quantitative
69 proteomics, we further show that FAP106 knockdown results in loss of conserved IJ MIP
70 structures and their corresponding proteins, as well as several MIP structures and proteins that
71 are lineage-specific. One of these, MC8, is demonstrated by cryoET to be a novel lineage-
72 specific *T. brucei* MIP and is required for parasite motility. Together, our results demonstrate
73 that FAP106 is a critical interaction hub required for assembly of conserved and lineage-specific
74 MIPs at the inner junction. This work advances understanding of MIP assembly mechanisms

75 and provides insight into parasite-specific MIPs that control *T. brucei* motility. Because they are
76 not present in the mammalian host, such MIPs are attractive for consideration as targets for
77 therapeutic intervention in trypanosome infections.

78 RESULTS

79 **FAP106 is required for parasite motility.**

80 FAP106 forms a 'tether loop' structure that spans the inner junction and is interconnected with
81 several other MIPs (13, 16, 20, 36). We used tetracycline-inducible RNAi (37) to deplete
82 FAP106 in procyclic form cells, hereafter referred to as "FAP106 KD". RNAi knockdown reduced
83 FAP106 mRNA expression by more than 95% (Fig. 1A) without affecting parasite growth rate
84 (Fig. 1B). FAP106 KD parasites did not exhibit any gross morphological defects, although their
85 flagella were shorter than normal (Fig. 1C-E). Notably, despite having a beating flagellum,
86 FAP106 KD parasites rarely exhibited directional motility, even at high cell densities, which
87 typically result in faster directional motility (Fig. 1F-G; Supp. Fig. S1). Thus, FAP106 is critical
88 for normal parasite motility.

89 **FAP106 is required for assembly of conserved and lineage-specific MIP structures.**

90 To determine whether FAP106 is required for assembly of other MIP structures, we performed
91 cryoET on purified, demembranated flagella from control and FAP106 KD parasites. Most
92 known MIPs assemble with a periodicity of 16, or 48 nm (9, 13-16, 20, 24, 36, 38) and we
93 therefore performed subtomogram averaging to determine the 48-nm repeating unit of the DMT
94 (Fig. 2; Supp. Fig. S2; Movie 1) for comparison to the published structures of the 48-nm repeat
95 from other organisms (13, 16, 20). MIP densities in the A-tubule appeared largely unaffected in
96 the FAP106 KD and, given the position of FAP106 in the B-tubule, we focused our analysis on
97 the B-tubule. Cross-sectional views of the cryoET tomogram show several major B-tubule MIP
98 densities are missing in the FAP106 KD. Although we do not have sufficient resolution to

99 identify the corresponding proteins directly, referencing the position of MIPs conserved in other
100 organisms provides insight. Longitudinal and cross-sectional views (Fig. 2C-D; Movie 1) show
101 loss of densities corresponding to the 'tether loop' structure of FAP106 in algae and mammals
102 (13, 16, 20) (Fig. 2B-C, red; Movie 1), consistent with the idea that FAP106 structure is
103 conserved across species (13). A density corresponding to the expected position of FAP52 (16,
104 20, 21) appears largely unaffected in the FAP106 KD (Fig. 2B-D, tan; Movie 1). We did not
105 resolve filamentous densities corresponding to FAP45 on protofilaments B6-B9 in other
106 organisms (13, 16), but these protofilaments were heavily decorated in *T. brucei* control cells
107 and relatively devoid of MIP densities in FAP106 KD (Fig. 2D; Movie 1). Additionally, densities
108 corresponding to the expected position of the FAP45 N-terminus are reduced in the FAP106 KD
109 (Fig. 2D, orange). Thus, FAP106 appears to be required for proper assembly of FAP45 but not
110 FAP52. Interestingly, the FAP106 KD also shows loss of FAP106-associated densities that
111 resemble FAP210 in other organisms (Fig. 2B, 2D, green; Movie 1; (13, 16, 20, 36)), although *T.*
112 *brucei* lacks a clear FAP210 homolog (Table 1). Overall, our results indicate FAP106 is critical
113 for assembly of a subset of B-tubule MIP structures in the vicinity of the IJ.

114 Beyond known MIP structures defined in other organisms, additional densities reduced
115 in the FAP106 KD correspond to MIP structures that are absent in one or more other organisms.
116 These lineage-specific MIP structures include a protruding density on protofilament B8, "MIP
117 B8", densities attached to protofilament A12, "MIP A12", and a protruding density on
118 protofilament B5, "MIP B5" (Fig. 2B). Thus, FAP106 is required for assembly of universally-
119 conserved, as well as lineage-specific MIPs.

120 **FAP106 is required for IJ filament assembly.**

121 The IJ filament is a conserved non-tubulin structure that connects protofilaments A1 and B10 in
122 organisms with cilia (8, 19). The IJ filament is comprised of PACRG and FAP20 subunits that
123 alternate each 4nm along the axoneme (4, 5). Interestingly, most organisms have a single hole

124 in the IJ filament every 96nm, corresponding to one missing PACRG subunit per 96-nm
125 repeating unit (8, 12, 38). *T. brucei* is unusual in having two holes per 96-nm repeating unit (15)
126 (Fig. 2E). The function of the IJ hole is not known, nor is the structural basis for the presence of
127 two holes per 96nm in *T. brucei*. Strikingly, our cryoET data show that loss of FAP106 results in
128 two additional holes per 48-nm repeat, giving six holes per 96-nm repeat (Fig. 2E; Movie 1).
129 These holes correspond to loss of every fourth subunit of the IJ filament (light blue in Fig. 2E),
130 which, based on analogy with *Chlamydomonas* (16), likely corresponds to PACRG.

131 **TMT proteomics identifies novel, FAP106-dependent, lineage-specific MIP proteins.**

132 To identify proteins corresponding to FAP106-dependent MIP densities, we used tandem mass
133 tag (TMT) quantitative proteomics to compare the protein composition of purified,
134 demembranated flagella from control and FAP106 KD parasites. We quantified more than 2500
135 proteins and only eight of these were significantly reduced in flagella from FAP106 KD parasites
136 ($\geq$2-fold reduced, adjusted p-value $\leq$0.06) (Fig. 3A; Table 2; Supp. Dataset S1). Three proteins
137 were observed to be increased in the knockdown (Fig. 3A; Supp. Dataset S1) and were not
138 studied further.

139 As expected, the protein most reduced in FAP106 KD parasites was FAP106 itself (Fig.
140 3A; Table 2), confirming efficient knockdown reported by qRT-PCR (Fig. 1A) and loss of
141 FAP106 protein from the axoneme (Fig. 2). Two other characterized proteins, FAP45 and
142 PACRG-B, were also reduced in the FAP106 KD (Fig. 3A-B, Table 2). FAP45 was almost 4-fold
143 reduced in FAP106 KD flagella (Fig. 3A; Table 2), supporting results from cryoET indicating
144 FAP106 is required for assembly of FAP45 into the axoneme (Fig. 2). FAP52 and FAP20 were
145 unaffected (Supp. Dataset S1), further supporting conclusions from cryoET that these proteins
146 assemble independently of FAP106 (Fig. 2). Notably, *T. brucei* has two PACRG homologs,
147 PACRG-A and PACRG-B (Table 1), which have been suggested to be functionally redundant
148 (39, 40). Despite a high degree of similarity, however, PACRG-A and PACRG-B are readily

149 distinguishable by mass spectrometry and our TMT proteomics analysis shows that only
150 PACRG-B is lost in the FAP106 KD (Fig. 3A; Table 2; Supp. Dataset S1). Loss of PACRG-B
151 and not PACRG-A indicates that the extra holes in the FAP106 KD (Fig. 2E) correspond to
152 missing PACRG-B subunits and demonstrates that PACRG-A and PACRG-B are not redundant.
153 Based on spacing of IJ subunits, the two IJ holes in control parasites most likely also
154 correspond to missing PACRG-B.

155 In addition to the known MIPs described above, five previously uncharacterized proteins
156 were reduced in flagella from FAP106 KD parasites (Fig. 3A; Table 2). One of these proteins
157 (RPC19, Tb927.11.8890) localizes to the nucleus (41), suggesting it is unlikely to be a MIP. The
158 remaining four proteins (Tb927.10.7120, Tb927.11.4920, Tb927.11.2770, and Tb927.3.3200),
159 are kinetoplastid-specific and localize to the flagellum (Supp. Fig. S3A; (41)), making them
160 strong candidates for lineage-specific, FAP106-dependent MIPs. Importantly, these four
161 proteins were separately identified as “MIP candidates”, MC3, MC5, MC8, and MC15, in a
162 completely independent APEX2-based proximity proteomics analysis as being nearby FAP45
163 and FAP52 in the B-tubule (Supp. Fig. S4; Supp. Dataset S2). Identification of these four
164 proteins by independent approaches greatly supports their potential as novel, kinetoplastid-
165 specific MIPs.

166 To test the requirement of MC3, MC5, MC8 and MC15 for flagellum structure and
167 function, we used tetracycline-inducible RNAi to individually knockdown each of these proteins.
168 Knockdown resulted in loss of the respective proteins from the flagellum (Supp. Fig. S3A)
169 without substantial effects on parasite growth. Loss of MC5 did not affect parasite motility, while
170 MC3, MC8, and MC15 are each required for normal motility (Fig. 3C; Supp. Fig. S3B). MC8 KD
171 and MC15 KD parasites also showed small reductions in flagellum length (Fig. 3D; Supp. Fig.
172 S3C). To ask whether additional proteins depend on these MCs for assembly into the axoneme,
173 we performed TMT proteomics on flagella isolated from parasites in which the individual MCs

174 were knocked down (Supp. Fig. S3D-G; Supp. Dataset S1). These proteomic analyses confirm
175 significant reduction of each MC in the respective knockdown, but no additional proteins were
176 lost (≥2-fold reduced, adjusted p-value ≤0.06) in any of the four knockdowns (Supp. Fig. S3D-G,
177 Supp. Dataset S1). Therefore, motility defects in MC3, MC8, and MC15 knockdowns reflect a
178 requirement for these individual, kinetoplastid-specific proteins in trypanosome motility.

179 **MC8 is a novel, lineage-specific *T. brucei* MIP that comprises the MIP B8 density.**

180 To identify MIPs corresponding to FAP106-dependent MIP densities, we fit the AlphaFold (42,
181 43) models of the above MCs into our cryoET structures. AlphaFold prediction of individual
182 proteins returned low-confidence predictions for MC3, MC5, and MC15, but predicted that MC8
183 folds into a structure with a high-confidence pyramid-like domain formed by α helices (Fig. 4A),
184 which fits well into the MIP B8 density (Fig. 4B). To determine whether MC8 in fact corresponds
185 to the MIP B8 density, we performed cryoET on purified, demembranated flagella from control
186 and MC8 KD parasites (Fig. 4C-E). Because TMT analysis showed that MC8 is the only protein
187 lost in the MC8 KD (Supp. Fig. S3F; Supp. Dataset S1), any density altered in the knockdown
188 must correspond to MC8 itself. The subtomographic average of the 48-nm repeating unit from
189 MC8 KD axonemes was nearly identical to that of controls except for the absence of the MIP B8
190 density (Fig. 4C-E). Thus, MC8 is a bona fide, *T. brucei*-specific B-tubule MIP that is required for
191 normal parasite motility (Fig. 3C; Supp. Fig. S3B). The motility defect of MC8 KD parasites, in
192 which the only missing protein is MC8, demonstrates importance of lineage-specific MIPs to
193 flagellar motility.

194

195 **DISCUSSION**

196 **FAP106 knockdown provides insights into MIP assembly mechanisms.**

197 Functional analysis lags behind identification and structural assignment of MIP proteins. Here
198 we combine functional, structural, and proteomic analysis to demonstrate that the conserved
199 MIP FAP106 is required for motility and is a key interaction hub for IJ filament and B-tubule MIP
200 structures. The role of FAP106 as a key interaction hub is emphasized by our finding that, while
201 FAP106 is required for assembly of FAP45 and lineage-specific MIP proteins MC3, 5, 8, and 15
202 (Fig. 2; Fig. 3, Fig. 5), loss of these individual proteins does not affect other MIP proteins or
203 structures (Supp. Fig. 3D-G; Fig. 4; Supp. Dataset S1; (21)). Thus, rather than interdependency,
204 our results suggest a hierarchical mechanism for B-tubule MIP assembly. FAP106-dependency
205 of FAP45 and a FAP210 structural homolog suggests that extensive interactions of FAP45 and
206 FAP210 with the tubulin lattice (13, 16) are relatively weak, while interactions with FAP106 (13)
207 are critical for stable binding and establishing their periodicity within the 48-nm repeat. This
208 supports the idea that an important role of MIPs is to enable complex assembly of proteins
209 along otherwise uniform protofilament polymers of tubulin (13, 14, 16) and suggests that loss of
210 FAP45 and FAP210 in RIB72 mutants (44) may reflect dependency on FAP106 rather than a
211 requirement for RIB72 directly. Our studies also provide a structural explanation for motility
212 defects of FAP106 mutants in trypanosomes (Fig. 2), and in sperm from FAP106/ENKUR
213 mutants in mice (35).

214 **The IJ filament subunit PACRG exhibits functional heterogeneity in trypanosomes.**

215 PACRG alternates with FAP20 to form the highly conserved IJ filament (4, 5). One of the more
216 mysterious features of DMTs is a hole in the IJ filament that occurs once per 96-nm repeat in
217 most organisms and corresponds to a missing PACRG (8, 12, 38). *T. brucei* is unusual in
218 having two IJ holes per 96-nm repeat, one at the site of nexin-dynein regulatory complex
219 (NDRC) attachment as observed in other organisms, and one proximal to the NDRC (15). The
220 proximal hole is devoid of external structures on the DMT (15), suggesting it is dictated by MIP
221 interactions rather than NDRC attachment, which is proposed for the NDRC hole (45). Our

222 findings support this idea, as loss of FAP106 results in extra holes in the IJ filament. Some
223 organisms have multiple PACRG homologs (24, 39, 46), but the contribution of individual
224 homologs is unknown. It is not known, for example, if they are distinctly incorporated within a
225 single axoneme or used for specialization of axoneme function in different cell types or
226 developmental stages. *T. brucei* has two PACRG homologs, PACRG-A and PACRG-B, which
227 have been suggested to be functionally redundant (39, 40). Our combined structural and
228 proteomics data instead support a model in which PACRG-A and PACRG-B both regularly
229 assemble within each IJ filament, alternating with FAP20 in turn, and with holes in the IJ
230 filament corresponding to missing PACRG-B, but not PACRG-A (Fig. 2E). Distinct locations and
231 assembly requirements for PACRG-A and PACRG-B indicate they play distinct roles in
232 assembly of the IJ. Although PACRG is conserved among ciliated organisms, the family of
233 PACRG proteins shows substantial heterogeneity in the N-terminal region that has been shown
234 to interact closely with the DMT lattice in *Chlamydomonas* (20, 46). Divergent N-termini of
235 PACRG-A versus PACRG-B may contribute to the differential dependence on FAP106 and their
236 distinct roles in assembly of the IJ.

237 **MC8 is a novel, lineage-specific T. brucei MIP that is required for parasite motility.**

238 The growing body of evidence suggests IJ subunits (PACRG and FAP20) and a core set of
239 conserved MIPs are found in all motile cilia, while other MIPs vary between organisms (13, 15-
240 17, 20, 24, 36, 38). FAP45, FAP52, and FAP106 represent core B-tubule MIPs while FAP126,
241 FAP276, and FAP210 are only found in some organisms (Table 1). MIP A12 densities (Fig. 2B-
242 C) are not present in *Chlamydomonas* or mammals (13, 16, 20) and appear more prominent in
243 *T. brucei* than MIP5a and MIP5b located at a similar position in *Tetrahymena* (9, 24, 36, 38), but
244 the proteins that comprise these densities remain unknown. We demonstrate that MC8 is a
245 bona fide lineage-specific MIP corresponding to the MIP B8 structure (Fig. 4). A density with
246 location and periodicity similar to MIP B8 is present in *Tetrahymena* (9, 24, 36, 38), but we were

247 unable to identify a *Tetrahymena* protein with sequence similarity to the MIP B8 protein, MC8.
248 Loss of MC8 in the FAP106 KD (Fig. 2B-2D) is likely due to loss of FAP45, which runs along
249 protofilaments B7-B8 (13, 16) and contacts FAP106 directly (13). Loss of MC8 compromises
250 motility (Fig. 3C; Supp. Fig. 3B) without affecting other MIPs (Fig. 4, Supp. Fig. 3F),
251 demonstrating that lineage-specific MIPs directly impact trypanosome motility. Validation of
252 MC8 as a bona fide *T. brucei* MIP in the current study, through a combination of mutant
253 analysis, structural, functional, and proximity proteomics approaches, demonstrates the power
254 of this combined approach for MIP identification and analysis. Our studies also strongly suggest
255 that MC3, 5, and 15 likewise correspond to novel, lineage-specific *T. brucei* MIPs. Trypanosome
256 motility is necessary for virulence in the mammalian host (33) and transmission through the
257 tsetse fly vector (34). Therefore, identification of novel, trypanosome-specific MIPs provides
258 attractive targets to consider for treatment of devastating diseases caused by these pathogens.

259 **Model for assembly of the IJ**

260 Our work provides an important advance toward elucidating the order of MIP assembly and
261 supports the following model for IJ assembly (Fig. 5). FAP20 binds every 8 nm, together with at
262 least a subset of PACRG, to form the IJ filament and this occurs independently from assembly
263 of FAP52 (20) and FAP106 (this work). FAP52 binds every 16 nm, independently of the IJ
264 filament (4) and FAP106 (this work), and may connect the IJ filament to the B-tubule via
265 FAP276 or other analogous structure (20, 36). FAP106 also binds every 16 nm, independently
266 from FAP52 (20), bridging the A- and B-tubules directly and serving as a critical guidepost for
267 assembling additional MIPs such as FAP45 and FAP210 (this work). Although FAP52 and
268 FAP106 bind regularly within each 48-nm repeat, their connections to other MIPs differ every 16
269 nm. Despite apparent contacts between FAP52 and other IJ MIPs (13, 16, 20, 36), assembly of
270 IJ MIPs in *Chlamydomonas* is largely unaffected by loss of FAP52 (20). Thus, while FAP52 and
271 FAP106 form contacts with each other and other IJ MIPs, they assemble independently from

272 one another, and FAP106 appears to be more critical for assembly of additional B-tubule MIPs.
273 Going forward, as additional MIPs are identified, particularly those that are lineage-specific,
274 application of combined proteomics, cryoEM, and mutant analysis, as done here, will be
275 necessary to completely define MIP assembly mechanisms and to yield a full understanding of
276 their contribution to flagellum function.

277

278 # MATERIALS AND METHODS

279 Biological materials are available from the authors upon request.

280 ***Trypanosoma brucei* culture**

281 Procyclic *T. brucei brucei* (strain 29-13) (47) were cultivated in SM medium (48) supplemented
282 with 10% heat-inactivated fetal bovine serum (FBS) at 28°C with 5% CO_2.

283 **In situ tagging**

284 mNeonGreen and APEX2-tagged cell lines were generated in the 29-13 background by C-
285 terminal tagging (41) with pPOTv6-puro-puro-mNG or pPOTv7-blast-blast-APEX2-3xHA,
286 respectively. pPOTv7-blast-blast-APEX2-3xHA contains the same APEX2-3xHA tag as in (49).
287 For MC3-NG, a transient CRISPR-Cas9 system (50) was used to tag both alleles. See Supp.
288 Table S2 for list of primers.

289 **Tetracycline-inducible knockdown**

290 Constructs for tetracycline-inducible knockdown were designed using RNAit (51) and cloned
291 into p2T7-177 (37). See Supp. Table S2 for list of primers. NotI-linearized plasmids were
292 transfected into 29-13 (FAP106 KD) or the corresponding MC-NG tagged cell lines (MC KDs)
293 using established methods (48). Clonal lines were generated by limiting dilution. Knockdown
294 was induced by growing cells in the presence of 1 µg/mL tetracycline (Tet) for at least 3d.
295 Control parasites were grown in the presence of tetracycline for comparison to the respective

296 KDs. For growth curves, cells were counted with a Beckman Coulter Z1 particle counter and
297 diluted daily to a concentration of 1e6 cells/mL, in triplicate.

298 **qRT-PCR**

299 Quantitative real-time PCR (qRT-PCR) was performed as previously described (52) with the
300 following modifications. FAP106-specific primers were designed using RNAit (51). Analyses
301 were performed in duplicate on three independent RNA preparations and values were
302 normalized to RPS23 (53). See Supp. Table S2 for list of primers.

303 **Motility analyses**

304 Cells were grown to ~1e6 cells/mL and loaded into polyglutamate-coated motility chambers (33)
305 sealed with Vaseline. 30s videos were acquired under dark-field illumination at ~40 frames per
306 second (fps) using a Hamamatsu ORCA-Flash 4.0 camera on a Zeiss Axio Imager A2 inverted
307 microscope with an EC Plan-Neofluar 10x/0.3 objective lens and Zen 2.6 Pro software. At least
308 five videos were collected for each independent biological replicate. Single cell tracking and
309 mean squared displacement were performed in MATLAB as previously described for fluorescent
310 parasites (33). For 'high density' motility analyses, cells were grown to ~1e7 cell/mL, then
311 diluted in conditioned medium to ~1e6 cells/mL and analyzed as above.

312 **Purification of demembranated flagella (detergent-extracted flagellum skeletons)**

313 Detergent extraction was done to demembranate flagellum skeletons, essentially as described
314 (15). Briefly, cells were washed in Dulbecco's PBS (DPBS), resuspended in Extraction buffer
315 (20 mM HEPES, pH 7.4, 1 mM $MgCl_2$, 150 mM NaCl, 0.5% NP40, 2x Sigmafast EDTA-free
316 protease inhibitor cocktail) for 15 min at room temperature, followed by depolymerization of
317 subpellicular microtubules with 1 mM $CaCl_2$ on ice for 30 min. Detergent-extracted flagellum
318 skeletons were pelleted at 1500 rcf for 10 min at 4°C.

319 **Flagellum length measurements**

320 For measurements of purified flagella, detergent-extracted flagellum skeletons were prepared
321 as described above and phase contrast images were acquired on a Zeiss Axioskop II

322 microscope with a Plan-Apochromat 63x/1.4 objective lens using Axiovision 4.8 software. For
323 measurements of the paraflagellar rod (PFR) in detergent-extracted cytoskeletons, cells were
324 washed in Dulbecco's PBS (DPBS) and allowed to adhere to glass cover slips for 10 min. Cover
325 slips were rinsed to remove unattached cells, then extracted with PEME buffer (100 mM PIPES,
326 2 mM EGTA, 1 mM $MgSO_4$, 0.1 mM EDTA, pH 6.8) + 1% IGEPAL CA-630 (NP40) + 2x
327 Sigmafast EDTA-free protease inhibitor cocktail for 10 min. Cover slips were fixed in methanol
328 at -20°C for 10 min, allowed to dry, then rehydrated in DPBS for 15 min. Cover slips were
329 blocked in DPBS + 8% normal donkey serum + 2% bovine serum albumin then incubated in
330 rabbit anti-PFR2 (54) primary antibody diluted 1:1000 in blocking solution, followed by donkey
331 anti-rabbit Alexa 594 secondary antibody diluted 1:1500 in blocking solution. Cover slips were
332 mounted in Vectashield containing DAPI and images were acquired on a Zeiss Axioskop II
333 fluorescence microscope with a Plan-Apochromat 100x/1.4 objective lens and Axiovision 4.8 or
334 Zen 3.5 Pro software. Flagellum lengths were measured in Fiji using the freehand line tool and
335 analyzed in GraphPad Prism 7.

336 **CryoET**

337 CryoET grids and detergent-extracted flagellum skeletons were prepared essentially as
338 described (15). Briefly, 2e8 log phase cells were harvested and washed twice in DPBS.
339 Flagellum skeletons were prepared as described above, resuspended in 100 ul Extraction buffer
340 and spun over a 30% sucrose cushion in Extraction buffer without NP40 at 800 rcf for 5 min at
341 4°C. 100-150 µL of flagellum skeletons were collected from the upper fraction, washed once
342 with 700 ul Extraction buffer, and once with 1 mL Extraction buffer without NP40. Flagellum
343 skeletons were resuspended in Extraction buffer without NP40 and vitrified on quantifoil grids
344 with 5nm fiducial gold beads.

345 With *SerialEM* (55), tilt series were collected in a Titan Krios instrument equipped with a
346 Gatan imaging filter (GIF) and a post-GIF K3 direct electron detector in electron-counting mode
347 with parameters listed in Table S1. Frames in each movie of the raw tilt series were aligned,

348 drift-corrected, and averaged with *Motioncor2* (56). The micrographs in each tilt series were
349 aligned and reconstructed into 3D tomograms by either weighted back projections (WBP, for
350 sub-tomographic averaging) or simultaneous iterative reconstruction technique (SIRT, for
351 visualization and particle picking) using the *IMOD* software package (57). The contrast transfer
352 function (CTF) was determined by *ctffind4* (58) and corrected with the *ctfphaseflip* program (59)
353 of *IMOD*.

354 **Sub-tomogram averaging, visualization and modeling**

355 4x binned SIRT reconstructed tomograms were further processed by IsoNet (60) to improve the
356 contrast for particle picking. Because of their distinct features, radial spokes were picked as
357 particles to represent the centers of 96nm axonemal repeat units. These particles for 96 nm
358 repeat units were subject to three rounds of rough alignments with PEET (7, 61). The particle
359 coordinates for 48-nm repeat units were generated from the coordinates of the aligned particles
360 for 96-nm repeat units. While keeping all coordinates for 96-nm repeat units, extra coordinates
361 for 48-nm repeat units were added unidirectionally from the 96-nm-repeat-units coordinates in a
362 distance of 48nm along the axonemal axis. PEET alignments were performed on the particles of
363 48-nm repeat units to generate the final maps. In Summary, the sub-tomographic averages of
364 flagellar components from four datasets were generated from the following number of particles:
365 1014 particles from 20 tomograms of Control dataset 1, 728 particles from 18 tomograms of
366 FAP106 KD dataset, 1936 particles from 52 tomograms of MC8 KD dataset, and 538 particles
367 from nine tomograms of Control dataset 2. The cryoET sub-tomographic averaged maps have
368 been deposited in the Electron Microscopy Data Bank under the accession codes EMD-28802,
369 EMD-28803, EMD-28804, and EMD-28805, for FAP106 KD, Control 1, MC8 KD, and Control 2,
370 respectively. The resolution of each sub-tomographic average was calculated by
371 *calcUnbiasedFSC* in *PEET* based on the 0.143 FSC criterion (Supp. Fig. S2).

372 UCSF ChimeraX (62) was used to visualize reconstructed tomograms and sub-
373 tomographic averages. For surface rendering with UCSF ChimeraX, maps were first low pass
374 filtered to either 20Å or 30Å.
375 Model prediction of MC8 was performed by AlphaFold Colab (42, 43). AlphaFold
376 predicted model of MC8 was superimposed into our averaged density with the molmap and
377 fitmap functions in UCSF ChimeraX.
378 **TMT labeling and quantitative proteomics**
379 Detergent-extracted flagellum skeletons were prepared from 2e8-4e8 log phase cells as
380 described above. After detergent extraction and depolymerization of subpellicular microtubules,
381 the pellet of flagellum skeletons was washed in Extraction buffer without NP40 and solubilized in
382 100 µl 8M urea, 100 mM Tris, pH 8 for 15 min at room temperature. Samples were centrifuged
383 at full speed for 15 min to pellet any insoluble material. The supernatant was diluted with 100
384 mM Tris, pH 8 to a final concentration of 2M urea and precipitated with 20% ice-cold
385 trichloroacetic acid (TCA) on ice overnight. The sample was centrifuged at full speed for 30 min
386 at 4°C and washed twice with -20°C acetone. The TCA-precipitated pellets were dried and
387 stored at ≤-20°C.
388 *Sample Digestion:* Protein pellets were resuspended with digestion buffer (8M urea, 0.1M Tris-
389 HCl pH 8.5). Each sample was normalized by absorbance at 280 nm and 25µg was aliquoted
390 for the digestion. Samples were reduced and alkylated via sequential 20-minute incubations
391 with 5 mM TCEP and 10 mM iodoacetamide at room temperature in the dark. Carboxylate-
392 modified magnetic beads (CMMB) also known as SP3 (63) and ethanol (50% final
393 concentration) were added to each sample to induce protein binding to CMMB beads. CMMB
394 beads were washed three times with 80% ethanol and then resuspended with 18ul of 100 mM
395 TEAB. Protein samples were digested overnight with 1ul of 0.1µg/ul LysC (Promega) and 2ul of
396 0.4µg/ul trypsin (Pierce) at 37 °C.

397 *TMT Labeling and CIF Fractionation:* 9ul of 100% acetonitrile were added to each sample to a
398 final concentration of 30% (v/v). Then the TMT labels were resuspended with 100% acetonitrile.
399 25ug of each sample was labeled using TMT6plex (Thermo Fisher Scientific) and the four
400 labeled samples of each set (two independent biological replicates each of control and
401 knockdown) were pooled. The pooled samples were fractionated by CMMB-based Isopropanol
402 Gradient Peptide Fractionation (CIF) method (64) into six fractions before mass spectrometry
403 (MS) analysis.
404 *LC-MS Acquisition and Analysis:* Fractionated samples were separated on a 75uM ID x 25cm
405 C18 column packed with 1.9µm C18 particles (Dr. Maisch GmbH) using a 140-minute gradient
406 of increasing acetonitrile and eluted directly into a Thermo Orbitrap Fusion Lumos mass
407 spectrometer where MS spectra were acquired using SPS-MS3. Protein identification was
408 performed using MaxQuant (65) v 1.6.17.0. against a user assembled database consisting of all
409 protein entries from the TriTrypDB (66) for *T. brucei* strain 927 (version 7.0). Searches were
410 performed using a 20 ppm precursor ion tolerance. TMT6plex was set as a static modification
411 on lysine and peptide N terminal. Carbamidomethylation of cysteine was set as static
412 modification, while oxidation of methionine residues and N-terminal protein acetylation were set
413 as variable modifications. LysC and Trypsin were selected as enzyme specificity with maximum
414 of two missed cleavages allowed. 1% false discovery rate was used as a filter at both protein
415 and PSM levels. Statistical analysis was conducted with the MSstatsTMT Bioconductor package
416 (67). Raw proteomic data have been deposited to the Mass Spectrometry Interactive Virtual
417 Environment (MassIVE) under accession ID MSV000090661.
418

419 ## ACKNOWLEDGMENTS

420 We thank Daniel Velez-Ramirez for technical assistance with APEX2 proximity proteomics and
421 Simon Imhof for helpful discussions. We also thank Astra Bryant for assistance with high speed

422 microscopy. Funding was provided by NIH grants AI052348 (K.L.H.), GM071940 (Z.H.Z), and
423 GM089778 (J.A.W). KJ was supported by the Beckman Scholars Program (Beckman
424 Foundation). We acknowledge the use of resources in the Electron Imaging Center for
425 Nanomachines supported by UCLA and grants from NIH (S10RR23057 and S10OD018111)
426 and NSF (DBI-1338135 and DMR-1548924).

427

428 **DATA AVAILABILITY STATEMENT**

429 The structure data generated during the current study have been deposited in the Electron
430 Microscopy Data Bank, accession codes EMD-28802, EMD-28803, EMD-28804, and EMD-
431 28805. The raw proteomics data generated during the current study have been deposited to the
432 Mass Spectrometry Interactive Virtual Environment (MassIVE) under accession IDs
433 MSV000090660 and MSV000090661 and the analyzed datasets are included in this published
434 article and its supplementary information files.

435

436 # REFERENCES

437 1. J. Wallmeier *et al.*, Motile ciliopathies. *Nat Rev Dis Primers* **6**, 77 (2020).
438 2. T. Kruger, M. Engstler, Flagellar motility in eukaryotic human parasites. *Semin Cell Dev Biol* **46**,
439 113-127 (2015).
440 3. H. S. Judelson, F. A. Blanco, The spores of Phytophthora: weapons of the plant destroyer. *Nat*
441 *Rev Microbiol* **3**, 47-58 (2005).
442 4. E. E. Dymek *et al.*, PACRG and FAP20 form the inner junction of axonemal doublet microtubules
443 and regulate ciliary motility. *Mol Biol Cell* **30**, 1805-1816 (2019).
444 5. H. A. Yanagisawa *et al.*, FAP20 is an inner junction protein of doublet microtubules essential for
445 both the planar asymmetrical waveform and stability of flagella in Chlamydomonas. *Mol Biol Cell*
446 **25**, 1472-1483 (2014).
447 6. H. Sui, K. H. Downing, Molecular architecture of axonemal microtubule doublets revealed by
448 cryo-electron tomography. *Nature* **442**, 475-478 (2006).
449 7. D. Nicastro *et al.*, The molecular architecture of axonemes revealed by cryoelectron
450 tomography. *Science* **313**, 944-948 (2006).
451 8. D. Nicastro *et al.*, Cryo-electron tomography reveals conserved features of doublet microtubules
452 in flagella. *Proc Natl Acad Sci U S A* **108**, E845-853 (2011).
453 9. M. Ichikawa *et al.*, Subnanometre-resolution structure of the doublet microtubule reveals new
454 classes of microtubule-associated proteins. *Nat Commun* **8**, 15035 (2017).
455 10. W. A. Anderson, R. A. Ellis, Ultrastructure of Trypanosoma Lewisi - Flagellum Microtublules and
456 Kinetoplast. *J Protozool* **12**, 483-& (1965).
457 11. K. Vickerman, On the surface coat and flagellar adhesion in trypanosomes. *J Cell Sci* **5**, 163-193.
458 (1969).
459 12. G. Pigino *et al.*, Comparative structural analysis of eukaryotic flagella and cilia from
460 Chlamydomonas, Tetrahymena, and sea urchins. *J Struct Biol* **178**, 199-206 (2012).
461 13. M. Gui *et al.*, De novo identification of mammalian ciliary motility proteins using cryo-EM. *Cell*
462 **184**, 5791-5806.e5719 (2021).
463 14. M. Ichikawa *et al.*, Tubulin lattice in cilia is in a stressed form regulated by microtubule inner
464 proteins. *Proc Natl Acad Sci U S A* **116**, 19930-19938 (2019).
465 15. S. Imhof *et al.*, Cryo electron tomography with volta phase plate reveals novel structural
466 foundations of the 96-nm axonemal repeat in the pathogen. *Elife* **8** (2019).
467 16. M. Ma *et al.*, Structure of the Decorated Ciliary Doublet Microtubule. *Cell* **179**, 909-922.e912
468 (2019).
469 17. M. Gui *et al.*, SPACA9 is a lumenal protein of human ciliary singlet and doublet microtubules.
470 *Proc Natl Acad Sci U S A* **119**, e2207605119 (2022).
471 18. P. Kiesel *et al.*, The molecular structure of mammalian primary cilia revealed by cryo-electron
472 tomography. *Nat Struct Mol Biol* **27**, 1115-1124 (2020).
473 19. S. Sun, R. L. Fisher, S. S. Bowser, B. T. Pentecost, H. Sui, Three-dimensional architecture of
474 epithelial primary cilia. *Proc Natl Acad Sci U S A* **116**, 9370-9379 (2019).
475 20. A. A. Z. Khalifa *et al.*, The inner junction complex of the cilia is an interaction hub that involves
476 tubulin post-translational modifications. *Elife* **9** (2020).
477 21. M. Owa *et al.*, Inner lumen proteins stabilize doublet microtubules in cilia and flagella. *Nat*
478 *Commun* **10**, 1143 (2019).
479 22. D. Stoddard *et al.*, Tetrahymena RIB72A and RIB72B are microtubule inner proteins in the ciliary
480 doublet microtubules. *Mol Biol Cell* **29**, 2566-2577 (2018).
481 23. T. Ide *et al.*, CFAP53 regulates mammalian cilia-type motility patterns through differential
482 localization and recruitment of axonemal dynein components. *PLoS Genet* **16**, e1009232 (2020).

483 24. S. Kubo *et al.*, Native doublet microtubules from Tetrahymena thermophila reveal the
484 importance of outer junction proteins. *bioRxiv* 10.1101/2022.09.30.510376,
485 2022.2009.2030.510376 (2022).
486 25. M. Rossi, G. Cicconofri, A. Beran, G. Noselli, A. DeSimone, Kinematics of flagellar swimming in
487 Euglena gracilis: Helical trajectories and flagellar shapes. *Proc Natl Acad Sci U S A* **114**, 13085-
488 13090 (2017).
489 26. J. L. Bargul *et al.*, Species-Specific Adaptations of Trypanosome Morphology and Motility to the
490 Mammalian Host. *PLoS Pathog* **12**, e1005448 (2016).
491 27. L. G. Wilson, L. M. Carter, S. E. Reece, High-speed holographic microscopy of malaria parasites
492 reveals ambidextrous flagellar waveforms. *Proc. Natl. Acad. Sci. USA* **110**, 18769-18774 (2013).
493 28. P. Buscher, G. Cecchi, V. Jamonneau, G. Priotto, Human African trypanosomiasis. *Lancet* **390**,
494 2397-2409 (2017).
495 29. K. I. Kasozi *et al.*, Prevalence of hemoprotozoan parasites in small ruminants along a human-
496 livestock-wildlife interface in western Uganda. *Vet Parasitol Reg Stud Reports* **17**, 100309 (2019).
497 30. L. Vincensini, T. Blisnick, P. Bastin, 1001 model organisms to study cilia and flagella. *Biol Cell* **103**,
498 109-130 (2011).
499 31. J. E. Donelson, M. J. Gardner, N. M. El-Sayed, More surprises from Kinetoplastida. *Proc Natl Acad*
500 *Sci U S A* **96**, 2579-2581 (1999).
501 32. T. Kruger, S. Schuster, M. Engstler, Beyond Blood: African Trypanosomes on the Move. *Trends*
502 *Parasitol* **34**, 1056-1067 (2018).
503 33. M. M. Shimogawa *et al.*, Parasite motility is critical for virulence of African trypanosomes. *Sci*
504 *Rep* **8**, 9122 (2018).
505 34. B. Rotureau, C. P. Ooi, D. Huet, S. Perrot, P. Bastin, Forward motility is essential for trypanosome
506 infection in the tsetse fly. *Cell Microbiol* **16**, 425-433 (2014).
507 35. M. K. Jungnickel *et al.*, The flagellar protein Enkurin is required for mouse sperm motility and for
508 transport through the female reproductive tract. *Biol Reprod* **99**, 789-797 (2018).
509 36. S. Li, J. J. Fernandez, A. S. Fabritius, D. A. Agard, M. Winey, Electron cryo-tomography structure
510 of axonemal doublet microtubule from. *Life Sci Alliance* **5** (2022).
511 37. B. Wickstead, K. Ersfeld, K. Gull, Targeting of a tetracycline-inducible expression system to the
512 transcriptionally silent minichromosomes of Trypanosoma brucei. *Mol Biochem Parasitol* **125**,
513 211-216 (2002).
514 38. K. Song *et al.*, In situ structure determination at nanometer resolution using TYGRESS. *Nat*
515 *Methods* **17**, 201-208 (2020).
516 39. H. R. Dawe, H. Farr, N. Portman, M. K. Shaw, K. Gull, The Parkin co-regulated gene product,
517 PACRG, is an evolutionarily conserved axonemal protein that functions in outer-doublet
518 microtubule morphogenesis. *J Cell Sci* **118**, 5421-5430 (2005).
519 40. R. Broadhead *et al.*, Flagellar motility is required for the viability of the bloodstream
520 trypanosome. *Nature* **440**, 224-227 (2006).
521 41. S. Dean, J. D. Sunter, R. J. Wheeler, TrypTag.org: A Trypanosome Genome-wide Protein
522 Localisation Resource. *Trends Parasitol* **33**, 80-82 (2017).
523 42. J. Jumper *et al.*, Highly accurate protein structure prediction with AlphaFold. *Nature* **596**, 583-
524 589 (2021).
525 43. M. Mirdita *et al.*, ColabFold - Making protein folding accessible to all. *bioRxiv*
526 10.1101/2021.08.15.456425, 2021.2008.2015.456425 (2022).
527 44. A. S. Fabritius *et al.*, Proteomic analysis of microtubule inner proteins (MIPs) in Rib72 null. *Mol*
528 *Biol Cell* **32**, br8 (2021).
529 45. T. Heuser, M. Raytchev, J. Krell, M. E. Porter, D. Nicastro, The dynein regulatory complex is the
530 nexin link and a major regulatory node in cilia and flagella. *J. Cell Biol.* **187**, 921-933 (2009).

531 46. N. Khan *et al.*, Crystal structure of human PACRG in complex with MEIG1 reveals roles in
532 axoneme formation and tubulin binding. *Structure* **29**, 572-586 e576 (2021).
533 47. E. Wirtz, S. Leal, C. Ochatt, G. A. Cross, A tightly regulated inducible expression system for
534 conditional gene knock-outs and dominant-negative genetics in *Trypanosoma brucei*. *Mol.*
535 *Biochem. Parasitol.* **99**, 89-101 (1999).
536 48. M. Oberholzer, M. A. Lopez, K. S. Ralston, K. L. Hill, Approaches for functional analysis of flagellar
537 proteins in African trypanosomes. *Methods in cell biology* **93**, 21-57 (2009).
538 49. D. E. Velez-Ramirez *et al.*, APEX2 Proximity Proteomics Resolves Flagellum Subdomains and
539 Identifies Flagellum Tip-Specific Proteins in Trypanosoma brucei. *mSphere* **6** (2021).
540 50. S. Shaw, S. Knusel, S. Hoenner, I. Roditi, A transient CRISPR/Cas9 expression system for genome
541 editing in Trypanosoma brucei. *BMC Res Notes* **13**, 268 (2020).
542 51. S. Redmond, J. Vadivelu, M. C. Field, RNAit: an automated web-based tool for the selection of
543 RNAi targets in Trypanosoma brucei. *Mol Biochem Parasitol* **128**, 115-118 (2003).
544 52. M. M. Shimogawa *et al.*, Cell Surface Proteomics Provides Insight into Stage-Specific Remodeling
545 of the Host-Parasite Interface in Trypanosoma brucei. *Molecular & cellular proteomics : MCP* **14**,
546 1977-1988 (2015).
547 53. M. A. Lopez, E. A. Saada, K. L. Hill, Insect stage-specific adenylate cyclases regulate social motility
548 in african trypanosomes. *Eukaryotic cell* **14**, 104-112 (2015).
549 54. E. A. Saada *et al.*, Insect stage-specific receptor adenylate cyclases are localized to distinct
550 subdomains of the Trypanosoma brucei Flagellar membrane. *Eukaryotic cell* **13**, 1064-1076
551 (2014).
552 55. D. N. Mastronarde, Automated electron microscope tomography using robust prediction of
553 specimen movements. *J Struct Biol* **152**, 36-51 (2005).
554 56. X. Li *et al.*, Electron counting and beam-induced motion correction enable near-atomic-
555 resolution single-particle cryo-EM. *Nat Methods* **10**, 584-590 (2013).
556 57. J. R. Kremer, D. N. Mastronarde, J. R. McIntosh, Computer visualization of three-dimensional
557 image data using IMOD. *J Struct Biol* **116**, 71-76 (1996).
558 58. A. Rohou, N. Grigorieff, CTFFIND4: Fast and accurate defocus estimation from electron
559 micrographs. *J Struct Biol* **192**, 216-221 (2015).
560 59. Q. Xiong, M. K. Morphew, C. L. Schwartz, A. H. Hoenger, D. N. Mastronarde, CTF determination
561 and correction for low dose tomographic tilt series. *J Struct Biol* **168**, 378-387 (2009).
562 60. Y.-T. Liu *et al.*, Isotropic Reconstruction of Electron Tomograms with Deep Learning. *bioRxiv*
563 10.1101/2021.07.17.452128, 2021.2007.2017.452128 (2021).
564 61. J. M. Heumann, A. Hoenger, D. N. Mastronarde, Clustering and variance maps for cryo-electron
565 tomography using wedge-masked differences. *J Struct Biol* **175**, 288-299 (2011).
566 62. T. D. Goddard *et al.*, UCSF ChimeraX: Meeting modern challenges in visualization and analysis.
567 *Protein Sci* **27**, 14-25 (2018).
568 63. C. S. Hughes *et al.*, Ultrasensitive proteome analysis using paramagnetic bead technology. *Mol*
569 *Syst Biol* **10**, 757 (2014).
570 64. W. Deng, J. Sha, K. Plath, J. A. Wohlschlegel, Carboxylate-Modified Magnetic Bead (CMMB)-
571 Based Isopropanol Gradient Peptide Fractionation (CIF) Enables Rapid and Robust Off-Line
572 Peptide Mixture Fractionation in Bottom-Up Proteomics. *Molecular & cellular proteomics : MCP*
573 **20**, 100039 (2021).
574 65. J. Cox, M. Mann, MaxQuant enables high peptide identification rates, individualized p.p.b.-range
575 mass accuracies and proteome-wide protein quantification. *Nat Biotechnol* **26**, 1367-1372
576 (2008).
577 66. M. Aslett *et al.*, TriTrypDB: a functional genomic resource for the Trypanosomatidae. *Nucleic*
578 *Acids Res.* **38**, D457-462 (2010).

579 67. T. Huang *et al.*, MSstatsTMT: Statistical Detection of Differentially Abundant Proteins in
580 Experiments with Isobaric Labeling and Multiple Mixtures. *Molecular & cellular proteomics :*
581 *MCP* **19**, 1706-1723 (2020).
582 68. J. Zhang *et al.*, Structure of the trypanosome paraflagellar rod and insights into non-planar
583 motility of eukaryotic cells. *Cell Discov* **7**, 51 (2021).

584

585

586 # FIGURES

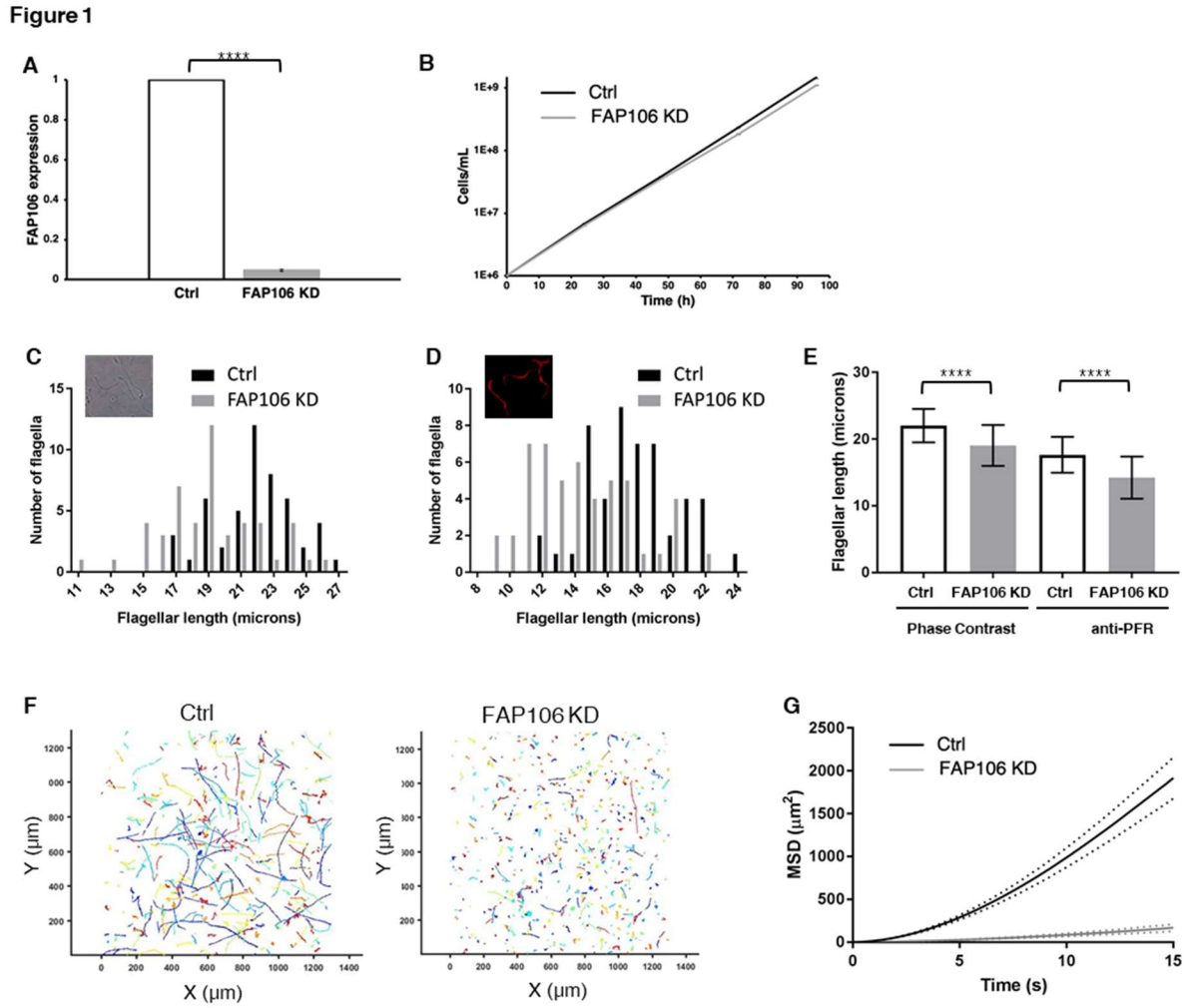

587

588 **Figure 1. FAP106 is required for parasite motility.** 29-13 (Ctrl) and FAP106 knockdown
589 (FAP106 KD) parasites were grown in the presence of tetracycline to induce knockdown. (*A*)
590 qRT-PCR analysis of FAP106 mRNA levels. Graph shows the mean ± standard deviation from
591 three independent biological replicates. **** Unpaired, two-tailed t-test p-value ≤ 0.0001. (*B*)
592 Cumulative growth curve shows the mean cell density vs time ± standard deviation from three
593 independent biological replicates. (*C*) Histogram shows the length distribution of purified,
594 demembranated flagella. Inset shows a representative phase contrast image. (*D*) Histogram
595 shows the distribution of flagellum lengths as measured by anti-paraflagellar rod (PFR)
596 immunofluorescence microscopy in detergent-extracted cytoskeletons. Inset shows a
597 representative image of detergent-extracted cytoskeletons with PFR in red. (*E*) Graph shows
598 the mean ± standard deviation of flagellum lengths in *C* (Phase Contrast) and *D* (anti-PFR).
599 Phase contrast: Ctrl = 22.0 ± 2.5 µm, FAP106 KD = 19.0 ± 3.1 µm; anti-PFR: Ctrl = 17.6 ± 2.7
600 µm, FAP106 KD = 14.2 ± 3.2 µm. N=50 flagella for each (*F*) Motility tracks of individual
601 parasites. (*G*) Mean squared displacement of parasites tracked in *F*. Dotted lines indicate the
602 upper and lower bounds of the standard error of the mean. Ctrl N=489; FAP106 KD N=675.
603 Data from an independent biological experiment are shown in Supp. Fig. S1.

Figure 2

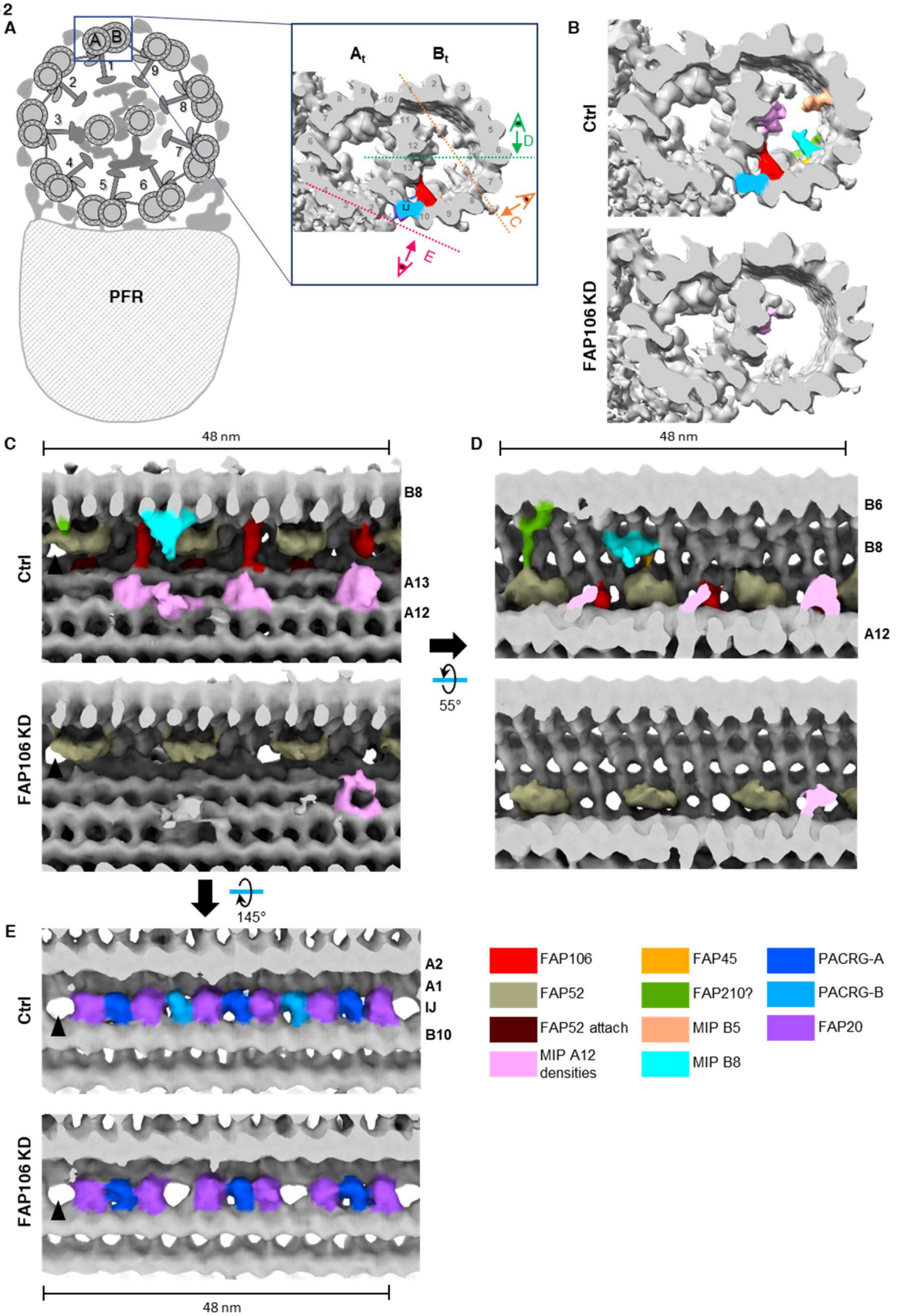
A
B
PFR
A_t
B_t
IJ
D
C
E
Ctrl
FAP106 KD
48 nm
B8
A13
A12
B6
55°
145°
A2
A1
IJ
B10
FAP106
FAP52
FAP52 attach
MIP A12 densities
FAP45
FAP210?
MIP B5
MIP B8
PACRG-A
PACRG-B
FAP20

604

605 **Figure 2. FAP106 is required for assembly of conserved and lineage-specific MIP**
606 **structures.** Demembranated flagella were purified from 29-13 (Ctrl) and FAP106 knockdown
607 (FAP106 KD) parasites grown in tetracycline to induce knockdown. Structure of the 48-nm
608 repeat of the DMT was obtained by cryoET, with subtomographic averaging. Densities are
609 colored according to the legend and based on similarity to published structures (13, 16, 20). (*A*)
610 Schematic illustrating a cross-section of the '9+2' axoneme and paraflagellar rod (PFR) viewed
611 from flagellum tip to base. Adapted from (68). Enlarged panel shows a single DMT, with A- and
612 B-tubules indicated (A_t, B_t) and protofilaments numbered. FAP106 (red) and the inner junction
613 filament (IJ) comprised of alternating PACRG (blue) and FAP20 (purple) are colored for
614 reference. Viewing angles shown in *C-E* are indicated. (*B*) Cross-sectional view of the DMT.
615 Colored densities indicate structures reduced or missing in FAP106 KD compared to Ctrl. (*C*
616 and *D*) Longitudinal views of the DMT. Viewing angles are indicated in *A, inset*. The 48-nm
617 repeat is indicated. Note that *T. brucei* has a structure similar to FAP210 of *Chlamydmonas*
618 (green) despite not having a clear FAP210 homolog (Table 1). (*E*) Longitudinal views of the
619 DMT, showing the IJ filament. Viewing angles are indicated in *A, inset.* The 48-nm repeat is
620 indicated. Black arrowheads indicate the position of the single hole found within each 48-nm
621 repeat in Ctrl DMTs. FAP20 and PACRG subunits are colored according to the legend, with
622 holes corresponding to missing PACRG-B subunits, as suggested by TMT proteomics (Figure
623 3).

624

Figure 3

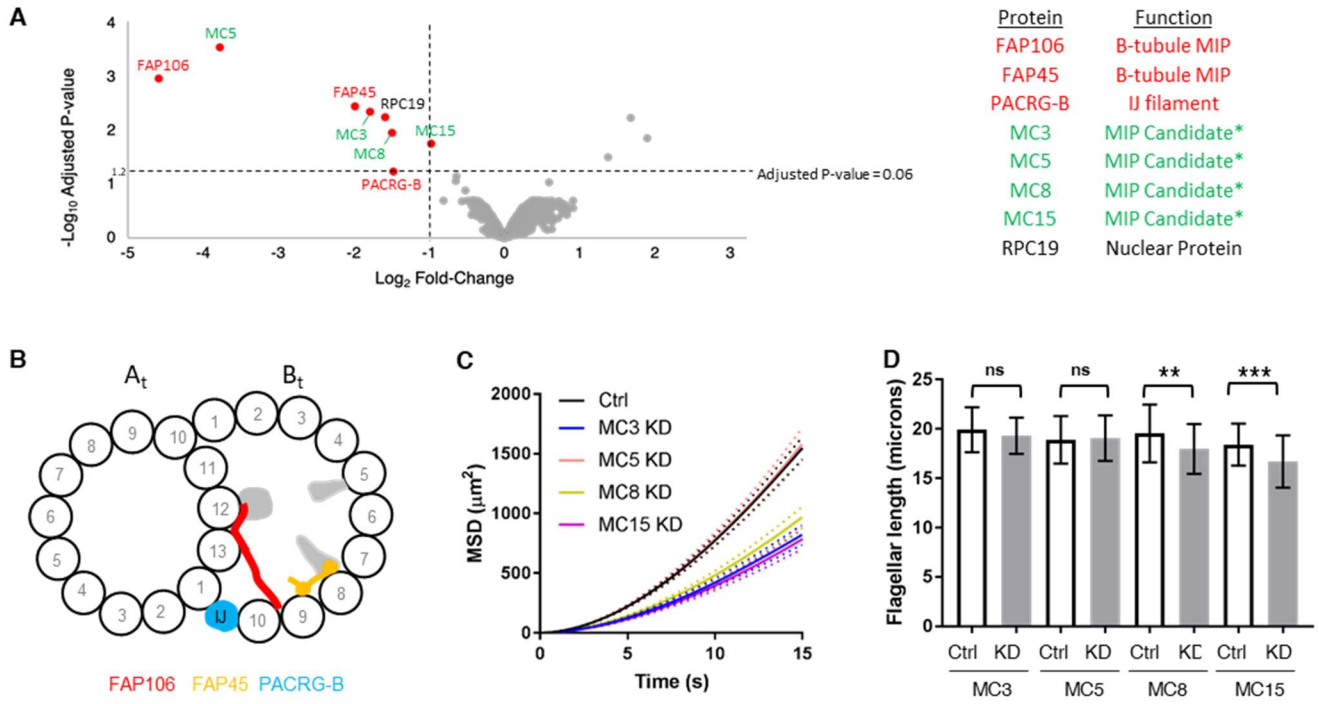

Figure 3. TMT proteomics identifies novel, FAP106-dependent, lineage-specific MIP proteins. (*A*) Demembranated flagella were purified from 29-13 (Ctrl) or FAP106 KD parasites grown in tetracycline to induce knockdown. Volcano plot shows significance (-Log_{10} Adjusted P-value) vs. relative abundance (Log_2 Fold-Change) for all proteins quantified by TMT proteomics. Relative abundance is calculated as FAP106 KD/Ctrl. Results are from two independent biological samples. Proteins that met the filtering criteria (2-fold decrease, adjusted P-value $\leq$0.06; Table 2; Supp. Dataset S1) are indicated by red dots. Labels indicate known proteins (red text) and putative MIP candidates (green text). Asterisks indicate proteins that were independently identified as putative B-tubule MIP candidates in a separate proximity labeling approach (Supp. Fig. S3; Supp. Dataset S2). (*B*) Cross-sectional view of the DMT as viewed from the flagellum tip, showing the positions of MIP structures lost in FAP106 KD as observed by cryoET (Fig. 2), with known MIPs colored. A- and B-tubules are indicated (A_t, B_t) and protofilaments are numbered. (*C*) Motility analysis showing mean squared displacement of 29-13 (Ctrl) and MC KD parasites from $\geq$2 independent biological replicates. Dotted lines indicate the upper and lower bounds of the standard error of the mean. Ctrl N=1761; MC3 KD N=627; MC5 KD N=753; MC8 KD N=709, MC15 KD N=751. Individual replicates are shown in Supp. Fig. S3B. (*D*) Detergent-extracted cytoskeletons were prepared from the indicated KD parasites or their respective mNeonGreen (NG)-tagged parental cell lines (Ctrl). Graph shows the mean $\pm$ standard deviation of flagellum lengths as measured by anti-PFR immunofluorescence microscopy. MC3-NG (Ctrl) = 19.9 $\pm$ 2.3 µm, MC3 KD = 19.3 $\pm$ 1.8 µm; MC5-NG (Ctrl) = 18.9 $\pm$ 2.4 µm, MC5 KD = 19.1 $\pm$ 2.3 µm; MC8-NG (Ctrl) = 19.6 $\pm$ 2.9 µm, MC8 KD = 18.0 $\pm$ 2.5 µm, MC15-NG (Ctrl) = 18.4 $\pm$ 2.1 µm, MC15 KD = 16.7 $\pm$ 2.6 µm. N=50 flagella for each, except N=45 flagella for MC15-NG. Unpaired, two-tailed t-test: ns = $p \geq 0.05$, ** = $p \leq 0.01$ and *** = $p \leq 0.001$.

651

Figure 4

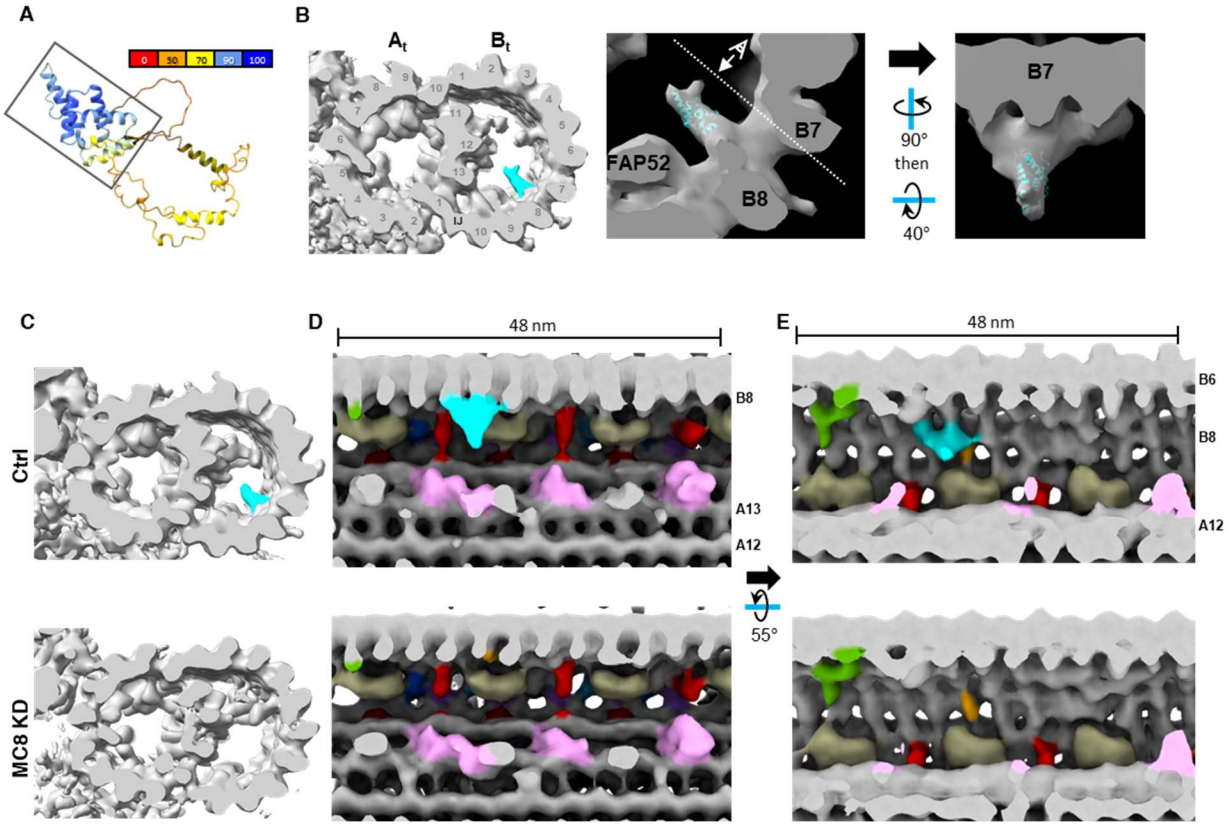

652

653 **Figure 4. MC8 is a novel, lineage-specific *T. brucei* MIP that comprises the MIP B8**
654 **density.** (*A*) AlphaFold prediction for MC8 (42, 43), colored according to confidence. Box
655 indicates high-confidence region modeled in *B*. (*B*) MC8 AlphaFold prediction modeled into MIP
656 B8 cryoET density. (*Left*) Cross-sectional view of the DMT, with the MIP B8 density colored
657 aqua. (*Middle, Right*) Enlarged view of MIP B8 density with AlphaFold prediction shown in aqua.
658 Viewing angle shown in *Right* panel is indicated by the dashed line in *Middle* panel. (*C-E*)
659 Demembranated flagella were purified from 29-13 (Ctrl) and MC8 knockdown (MC8 KD)
660 parasites grown in tetracycline to induce knockdown. Structure of the 48-nm repeat of the DMT
661 was obtained by cryoET, followed by subtomographic averaging. (*C*) Cross-sectional view of the
662 DMT with MIP B8 density colored in aqua. (*D* and *E*) Longitudinal views of the DMT. Viewing
663 angles and colors are as indicated in Fig. 2.

664

Figure 5

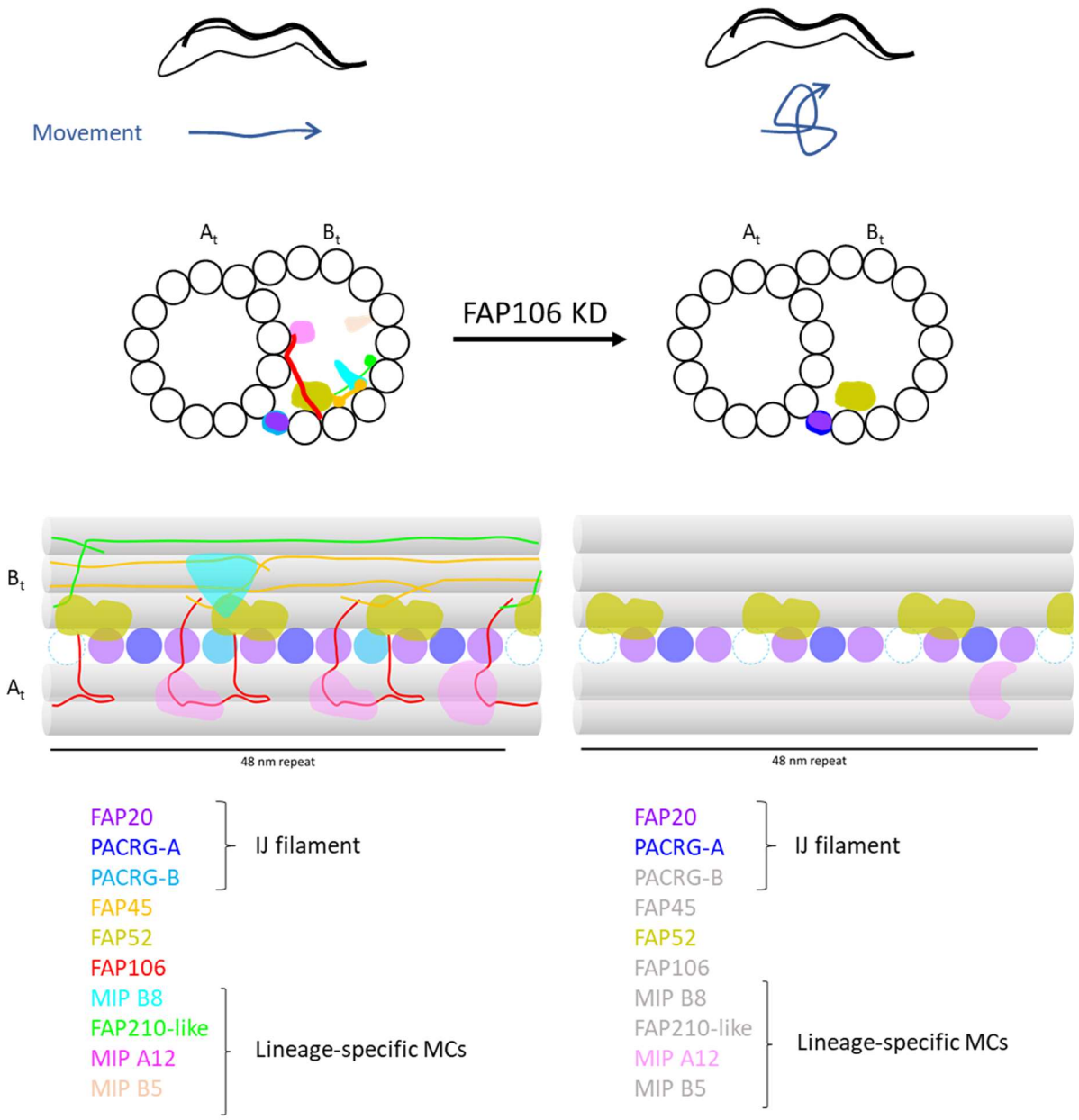

Figure 5. FAP106 is required for parasite motility and assembly of conserved and lineage-specific MIPs at the inner junction. Normal parasite motility relies on FAP106 as a critical interaction hub for assembly of MIPs at the inner junction (IJ). Cross-sectional and longitudinal views of the DMT are illustrated. Conserved IJ MIPs PACRG-A, FAP20 and FAP52 assemble independently of FAP106, however PACRG-B does not stably assemble into the IJ filament without FAP106. The B-tubule remains intact and connected to the A-tubule at the IJ, despite loss of multiple IJ MIPs. FAP106 is also critical for assembly of the conserved MIP, FAP45, and a FAP210-like protein (modeled as filaments based on published structures (13, 16, 20)), as well as several novel, lineage-specific MIPs.

675 ## Movie Legends

676 **Movie 1. Subtomographic average of the 48-nm repeat.** Video showing 3D reconstruction of
677 48-nm repeat from 29-13 (Control) and FAP106 KD DMTs, rotating between views shown in Fig
678 2.

679 **Table 1. Known B-tubule MIPs**

Chlamydomonas	Mammals	*Tetrahymena*	*Trypanosoma*
†PACRG	PACRG	TTHERM_00446290; TTHERM_00499310; TTHERM_00499570	Tb927.3.2310; Tb927.9.9940
†FAP20	CFAP20	TTHERM_00418580	Tb927.10.2190
FAP45	CFAP45	TTHERM_001164064	Tb927.8.4580
FAP52	CFAP52	TTHERM_01094880	Tb927.11.7560
FAP106	ENKUR	TTHERM_00137550; TTHERM_00370750	Tb927.11.4880
FAP77	CFAP77	TTHERM_00974270; TTHERM_01190430	
FAP210	CFAP210	TTHERM_00643530	
FAP90	CFAP90		
FAP126	Flattop		
FAP144	FAM183A		
FAP276	CFAP276		
FAP112		TTHERM_00884620	
	EFCAB6		
	SPACA9		
			Tb927.11.2770 (MIP B8, this study,‡)

680

681 †FAP20 and PACRG form the IJ filament

682 ‡Corresponding structure was called 'MIP3c' in (15) but our current study suggests this structure
683 is distinct from MIP3c (FAP45).

684

685 **Table 2. Proteins significantly reduced in FAP106 KD flagellum skeletons by TMT**
686 **proteomics**

Gene	Gene ID	Fold Reduction	Adjusted P-value	Protein Localization	Function
FAP106	Tb927.11.4880	24.02	0.0011	Flagellum	B-tubule MIP
FAP45	Tb927.8.4580	3.95	0.0035	Flagellum	B-tubule MIP
PACRG-B	Tb927.9.9940	2.77	0.0576	Flagellum	IJ filament
MC5	Tb927.11.4920	13.74	0.0003	Flagellum	MIP candidate*
MC3	Tb927.10.7120	3.44	0.0044	Flagellum	MIP candidate*
MC8	Tb927.11.2770	2.81	0.0111	Flagellum	MIP candidate*
MC15	Tb927.3.3200	1.95	0.0177	Flagellum	MIP candidate*
RPC19	Tb927.11.8890	2.99	0.0055	Nucleus	RNA polymerase

687

688 *Identified by independent APEX2-based proximity proteomics of known B-tubule MIPs (see
689 Supp. Dataset S2)

690